

Effect of Slag-Steel Reaction on the Initial Solidification of Molten Steel during Continuous Casting



WANLIN WANG, ZHICAN LOU, and HAIHUI ZHANG

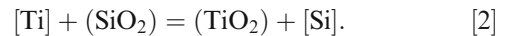
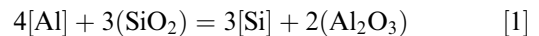
With the mold simulator technique, the effect of slag-steel reaction on the initial shell solidification as well as the heat transfer and lubrication behavior of the infiltrated mold/shell slag film was studied in this article. The results showed that the Al_2O_3 content, the CaO/SiO_2 ratio, and the viscosity of mold flux were increased with the progress of the slag-steel reaction during casting. The slag-steel reaction has two major effects on the initial shell solidification: one is increasing the mold heat flux and shell thickness by the decrease of slag film thickness. The other is the reduction of mold heat flux by the increase of crystal fraction in slag film. Mold flux with a lower basicity, viscosity, and crystallization temperature would result in a larger liquid slag consumption and the uneven infiltration of slag into the mold and shell gap that eventually leads to the irregular solidification of initial shell with a poor surface quality, such as slag entrapment and depressions as well as glaciation marks. Conversely, mold flux with a higher viscosity, basicity, and crystallization temperature would result in a smaller liquid slag consumption, which would cause the poor mold lubrication, the longitudinal shell surface defects, and drag marks.

<https://doi.org/10.1007/s11663-018-1245-4>

© The Minerals, Metals & Materials Society and ASM International 2018

I. INTRODUCTION

DURING the continuous casting, mold flux is usually added on the top of molten steel surface to protect the steel from oxidation, moderate the mold heat transfer, absorb the inclusions rise from molten steel, lubricate the newly formed shell, and control the heat transfer between the shell and the mold.^[1] The contents of Al_2O_3 and TiO_2 were found to increase in the mold flux with the progress of continuous casting of Interstitial-free (IF) steels (Ti-bearing, Al-killed ultra-low carbon steel).^[2] The sources of Al_2O_3 and TiO_2 pickup were partly from the absorbed inclusions of Al_2O_3 and TiO_2 (original from steelmaking) rising from molten steel; however, the majority was from the reaction between the silica in liquid slag and the alloying element in molten steel as shown in the following equations:



The pickup of Al_2O_3 content would lead to the increase of the break temperature (T_{br}), solidification temperature, fraction of crystalline phase (f_{cryst}), and viscosity (μ_s) of mold flux, and then introduce the reduction of slag consumption ($Q_{\text{slag}} = 0.55/\mu_s^{0.5} \cdot V_c$ or $Q_{\text{slag}} = 0.6/\mu_s \cdot V_c$).^[3] Additionally, with the increase of Al_2O_3 and TiO_2 in the spent mold flux, the most common crystal cuspidine ($\text{Ca}_4\text{Si}_2\text{O}_7\text{F}_2$) would partly be replaced by nepheline ($\text{NaAlSi}_3\text{O}_8$) and gehlenite ($\text{Ca}_2\text{Al}_2\text{SiO}_7$).^[3,4] Once the amount of alumina exceeds a critical value (about 15 to 20 wt pct), the serious operational problems, such as poor mold lubrication, severe slag rim formation, surface defects, sticking, and breakouts, would arise.^[3,5-7] Thus, the clear understanding of the effect of slag-steel reaction on mold flux performances during continuous casting would be of great importance for the control of the quality of final slab.

Previous works suggested that the thickness of the liquid slag film (d_l) between the oscillating mold and the solidifying shell determines mold lubrication, where an increase of break temperature and solidification temperature of mold flux would lead to a reduction of d_l that could deteriorate the mold lubrication.^[8]

WANLIN WANG, ZHICAN LOU, and HAIHUI ZHANG are with the School of Metallurgy and Environment, Central South University, Changsha 410083, Hunan, China. Contact e-mail: zhanghaihuiemail@gmail.com

Manuscript submitted August 10, 2017.

Article published online March 20, 2018.

Additionally, mold heat flux is usually decreased with increasing the thickness of solid slag film (d_s) and f_{crys} .^[9] Moreover, crystallization of slag film will decrease the heat transfer by scattering radiation at the grain boundaries,^[10–15] and lead to the formation of interfacial thermal resistance (R_{int}) between the mold and the slag film.^[16] In practice, R_{int} increases with increasing f_{crys} and d_s .^[17,18] Works by Esaka^[19] and Yamauchi *et al.*^[20] indicated that the thickness of infiltrated mold/shell slag film decreased with increasing the basicity (CaO/SiO₂) and solidification temperature of mold flux. Hanao *et al.*^[21] has investigated the heat transfer behavior of slag film at meniscus area during continuous casting of hypo-peritectic steel by a pilot castor. He found that the thickness of the slag film decreased with the increase of slag basicity but showed no correlation with slag solidification temperature, while the mold heat flux decreased with the increase of f_{crys} and solidification temperature and showed no correlation with the thickness, viscosity, and basicity of slag film. However, a statistical analysis on the plant data^[22] and numeric model^[8] indicated that mold heat flux increased with increasing slag viscosity, and/or decreased with increasing T_{br} . Therefore, there is still inconsistency in the report regarding the exact effects of slag viscosity and basicity on the mold heat flux.

To limit the reaction between Al in steel and Si in mold flux during the continuous casting of high-aluminum steels, industrial caster trials^[23,24] and mold simulator trials^[25–32] were conducted to evaluate or develop new mold flux for a better shell surface quality. For example, Cho *et al.*^[23,24] compared the lime-silica and lime-alumina-based mold fluxes for continuous casting of high-aluminum steels using a pilot caster, and found the lime-alumina mold flux could reduce the alumina pickup to less than 5 pct in comparison with 15 pct alumina pickup in lime-silica mold flux. However, it is not always feasible to conduct experiments on an industrial continuous caster for the development of mold flux. Therefore, the mold simulator technique was developed to assess the effect of mold flux performance on the shell surface quality under laboratory conditions.^[25,26] For example, works by Sohn *et al.*^[27,28] and Wang *et al.*^[29–31] had conducted mold simulator simulations, and suggested that the crystallization of the infiltrated mold/shell slag film is dynamic, and f_{crys} increases as the slag film is sustained at high temperatures for a longer period. However, the effect of slag-steel reaction on the surface profile and solidification of initial steel shell, as well as the heat transfer and lubrication behavior of the infiltrated mold/shell slag film during continuous casting of IF steel is still not fully understood.

In this study, the effects of the accumulation of Al₂O₃ and TiO₂ in mold flux on the initial shell solidification, and the heat transfer and lubrication behaviors of the infiltrated mold/shell slag film during the continuous casting of IF steels were assessed using a mold simulator. Firstly, four mold simulator trials were designed to simulate the initial shell solidification in the continuous casting mold. Those four trials are corresponding to four different times of 5, 12, 20, and 25 minutes after

adding the mold flux on the top of molten steel, respectively, while the (pct Al₂O₃) and CaO/SiO₂ ratio in mold flux increased successively as the reaction between mold flux and molten steel progressed. Then the effect of the slag-steel reaction on the initial shell solidification as well as the heat transfer and lubrication behavior of the infiltrated mold/shell slag film was investigated.

II. EXPERIMENTAL APPARATUS AND PROCESS

A. Experimental Apparatus

The mold simulator applied to this study is an inverse-type water-cooled copper mold (30 mm × 50 mm × 350 mm) with oscillation ability and is shown in Figure 1. A U-type water-cooling groove with 10 mm diameter is manufactured inside the mold that consists of one water inlet and one water outlet at quarter-width and three-quarter-width positions of mold, respectively. The copper mold is equipped with an extractor that makes only one face of the mold exposed to the liquid melt. As the molten steel contacts the mold surface and forms the initial shell, the extractor withdraws the solidifying shell downward and makes the fresh molten steel contact with mold for subsequent solidification that is similar to what the dummy bar does at the start-up of a continuous casting. The responding mold temperatures during casting are measured by a fast thermal monitoring system at the sampling rate of 60 Hz, which consists of 16 highly sensitive T-type thermocouples. As shown in Figure 1, along the centerline of mold, two columns of T-type thermocouples (2 × 8) are embedded at different depth inside the mold wall. Two columns of thermocouples are spaced 3 and 8 mm away from the mold surface, respectively, and the dot points represent the fixed locations of thermocouples' tips.

B. Experimental Procedure

The brief operational steps of the mold simulator run were as follows. *First*, about 20 kg of IF steel (the composition of Ti-bearing, Al-killed ultra-low-carbon steel is analyzed by plasma-atomic emission spectrometry (ACROS, SPECTRO) and listed in Table I) was melted in an induction furnace (MgO lining) in argon atmosphere (with purify of 99.99 pct). *Next*, the temperature of the melt was adjusted to the target value (to control the superheat); the metal Al (~ 100 g) as a deoxidizer was added to the molten steel. The mold flux (~ 0.5 kg, composition listed in Table II, before the experiment the added mold flux has been decarburized by placing it into a furnace to avoid the C pickup in molten steel during the casting) designed for IF steel was added to the surface of molten steel, so that there would be a layer of molten flux 6 to 9 mm thick on the top of molten steel (the selected thickness of liquid slag layer could be comparable to that thickness of liquid slag on the mold top of an industrial continuous casting mold). When the target slag-steel reaction time elapsed, the

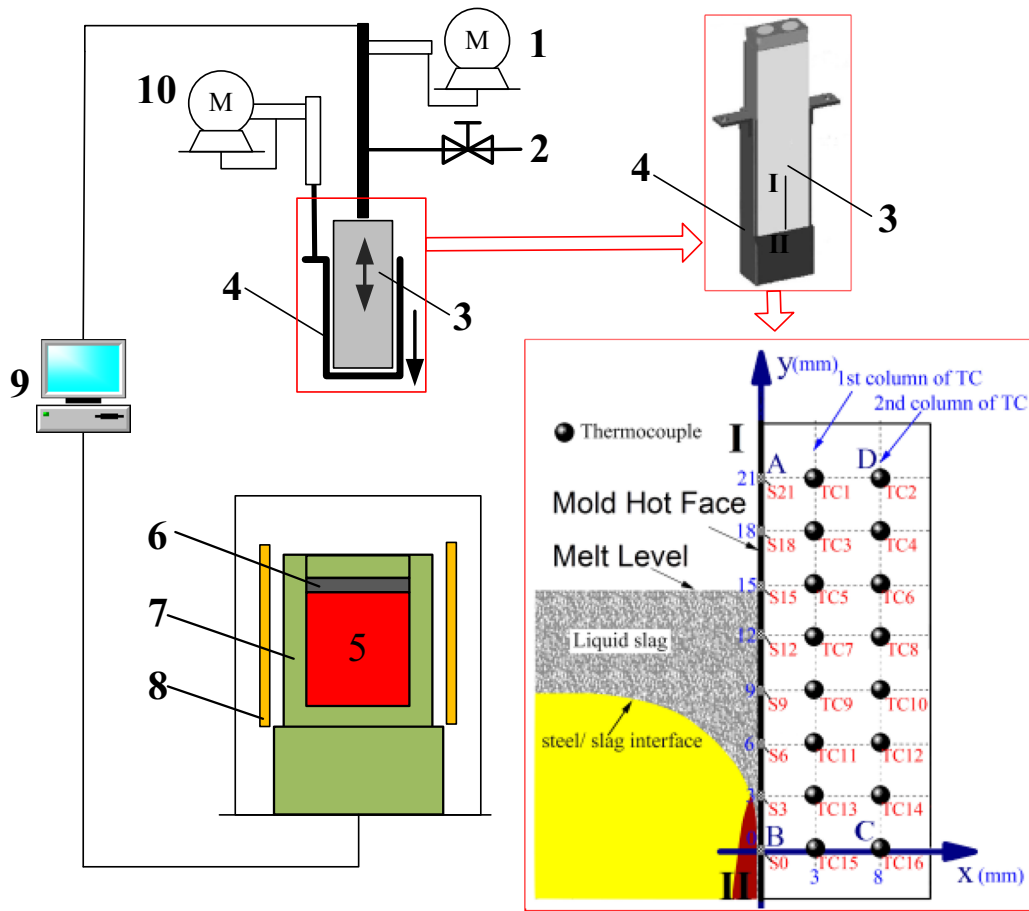


Fig. 1—Schematic of the mold simulator and locations of the thermocouples in the mold wall: 1-oscillation drive; 2-cooling water; 3-mold; 4-extractor; 5-melt; 6-mold flux; 7-induction furnace; 8-induction coil; 9-data acquisition and control system; 10-extractor drive.

mold covered with extractor was descended toward the melt, while the mold was kept oscillated. The mold and extractor were lowered to the preset depth into the melt bath so that the liquid mold flux surface and the meniscus of molten steel would be located in the mold thermocouple-measuring zone. After the mold and extractor reached the target location, it was held for 5 seconds to form an initial shell on the mold to ensure the initial shell is strong enough to prevent tearing during extraction. Then, the extractor withdrew the solidifying shell downward at a given casting speed, while the mold moved upward at a certain speed to compensate for the rise of mold level, so that the liquid mold flux surface and meniscus could be kept at the same position with respect to the mold. When the casting was completed for the desired length, the mold and extractor were withdrawn out of the furnace and then cooled in the air. Subsequently, the position of shell tip with respect to the mold was measured, and the solidified shell and the slag film adjacent to mold were cut away for the further study. Finally, the measured temperatures were delivered to a Two-Dimensional Inverse Heat Conduction Problem (2D-IHCP) mathematic model,^[33] and then the heat flux and temperature on the mold surface were recovered. In Figure 1, rectangle ABCD is the computational domain of

2D-IHCP model, where AB is the mold surface that close to the hot shell and CD is another side that close to the cooling channel. The 2D-IHCP model could determine the mold surface heat flux from the limited number of in-mold wall temperature measurements using Conjugate Gradient Method to find a heat flux function that approaches to the real boundary heat flux, and the detailed description of this mathematic model has been well illustrated in our previous study.^[33]

To measure the shell thickness, Fe-S alloy was added into the molten steel just before the end of casting. After the casting, the slab was cut along the centerline of mold. By analyzing the result from the sulfur print of the longitudinal section of the shell, the white area was regarded as the solidified shell formed before the Fe-S alloy addition. Finally, the shell thickness was measured by a Vernier micrometer.

III. RESULTS AND DISCUSSION

In the present work, four different mold simulator trials of E1, E2, E3, and E4 were conducted successively, where those four trials corresponding to 5, 12, 20, and 25 minutes after adding mold flux on the top of molten steel, respectively. Those experimental times selected are

Table I. Chemical Compositions of Steel (Weight Percent)

C	Si	Mn	P	S	Al	Ti	Nb
0.0008	0.005	0.107	0.0113	0.0041	0.0335	0.0189	0.0112

Table II. Chemical Composition and Physical Properties of Mold Fluxes

NO	Chemical Composition (Wt Pct)									Viscosity at 1300 °C, μ_0 (Pa s)	Viscosity exponent, n	Crys. Temp, T_{sol} (K)
	CaO	SiO ₂	Al ₂ O ₃	F	MnO	MgO	TiO ₂	Fe ₂ O ₃	Basicity			
Orin	36	37.5	6	6	7	0	—	—	0.96	0.27	1.6	1417
E1	35.72	35.16	7.62	5.61	0.96	3.5	0.24	2.54	1.02	0.35	1.6	1427
E2	35.53	34.12	10.34	4.56	1.20	3.33	0.58	4.19	1.04	0.47	1.5	1473
E3	35.40	33.00	13.50	3.50	1.50	5.53	0.80	5.04	1.07	0.58	1.5	1485
E4	35.40	32.25	14.56	3.80	1.64	5.90	0.92	5.16	1.10	0.76	1.2	1513

Table III. Experimental Parameters During the Casting Process

Oscillation frequency, f (Hz)	2.08
Oscillation amplitude, A (mm)	4.9
Casting speed, V_c (m/min)	0.72
Casting temperature, [K (°C)]	1875 (1575)

because about 1200 seconds (= 20 minutes) is needed for the reaction $4[Al] + 3(SiO_2) = 3[Si] + 2(Al_2O_3)$ to achieve the state of equilibrium.^[23,34] The casting parameters, such as the casting temperature, casting speed, mold oscillation frequency, and amplitude are listed in Table III. After each of trial, the mold flux was sampled and its chemical composition was analyzed by X-ray fluorescence. The chemical compositions of sampled mold fluxes for **E1**, **E2**, **E3**, and **E4** trials as well as the composition of mold flux before experiment are listed in Table II. It could observe the content of Al₂O₃ in slag increased dramatically from the original 6 to 7.26 pct, 10.34, 13.50, and 14.56 pct for **E1**, **E2**, **E3**, and **E4**, respectively, which is mainly attributed to the reaction between Al in steel and Si in mold flux. Also, the content of TiO₂ in slag increased slightly which may be associated with the reaction between Ti in steel and Si in mold flux and the absorbed TiO₂ inclusions from molten steel. Besides, the mass ratio of CaO/SiO₂ increased from the original 0.96 to 1.02, 1.04, 1.07, and 1.10 for **E1**, **E2**, **E3**, and **E4** trials, respectively, owing to the fact that the slag-steel reactions occur at cost of SiO₂ in mold flux. Furthermore, MgO content increased from the original zero to 3.50, 3.33, 5.53, and 5.90 pct for **E1**, **E2**, **E3**, and **E4**, respectively, owing to the dissolution of MgO at the slag line from the induction furnace.

The temperature-dependent viscosities of slag before and after experiments were measured using a Brookfield DV-II+ viscometer (Brookfield Inc.) through the rotating cylinder method. Viscosity-temperature ($\mu_s - T$) data of slag are fitted to the function $\mu_s = \mu_0 \times [(1300 - T_{sol}) / (T - T_{sol})]^n$, where μ_0 is the viscosities of slags at 1300 °C and n is temperature-dependent viscosity exponent. While the crystallization

temperature of slag (T_{sol}) equals to the interfacial temperature between the crystal and liquid layers was measured by an experiment by SHTT.^[35–37] Then the measured viscosity of slag at 1300 °C, viscosity exponent (n), and crystallization temperature of slag (T_{sol}) are listed in Table II. The slag viscosity (μ_s) increased from the original 0.27 to 0.35, 0.47, 0.58, and 0.76 Pa s, and the crystallization temperature (T_{sol}) increased from the original 1417 to 1427, 1473, 1485, and 1513 K for **E1**, **E2**, **E3**, and **E4**, respectively.

A. Surface Profiles of Shells

After the casting and shell has completely cooled, the solidified shell was cut away from mold. The shell was removed from the mold, and the pieces of slag film were taken out from the mold-shell gap and then fitted altogether like a puzzle. Figure 2 shows the images of the shells and the infiltrated mold/shell slag films from the trials of **E1**, **E2**, **E3**, and **E4**, respectively. For trial **E1**, the initial shell surface is general smooth with ripples appearing on the surface, and slag film obtained in **E1** test shows a large integrated piece suggesting a good infiltration during the mold simulator trial. Small area near the edge of shell surface is observed to wrap tiny slag particles (labeled **A**), which may be due to the fact that mold-level fluctuation was observed and the liquid slag seemed to be trapped into the mold and shell gap during the casting. For trial **E2**, the shell surface appears obvious depression and glaciation marks (labeled **B**), and the thickness of slag film is irregular (see Figure 5). The formation of glaciation marks on shell profile may be associated with the irregular infiltration of slag into the mold and shell gap and the uneven solidification of initial shell. For trial **E3**, obvious wave surface with regular deep oscillation marks are appearing on the shell surface. For trial **E4**, the shell surface exhibits irregular oscillation marks and significant ripples, and the drag marks are clearly appearing at the top right side (as labeled **C**) due to the insufficient lubrication. The slag film obtained from this case is fragmented that is introduced by the lack of liquid slag infiltration between mold and shell. Besides, obvious slag entrapment under the surface defects is clearly observed for **E2** to **E4** trials.

The detailed discussion about the slag infiltration and shell solidification would be given later.

B. Shell Solidification

Figure 3 shows the longitudinal sections of the solidified shells along the centerline of mold for the trials **E1**, **E2**, **E3**, and **E4**, respectively, where the top of those shells exhibited a carve shape due to the frozen meniscus of each shell.

The measured shell thickness (d_{shell}) by a Vernier micrometer of each trial is shown in Figure 4. The shell thickness (d_{shell}) is fitted to a square root function, $d_{\text{shell}} = K \cdot t_s^{1/2}$, where the solidification time (t_s , second) is calculated using the equation $t_s = l/V_c$ (l is the distance from the shell tip, and V_c is the casting speed), and Adj. R^2 is adjusted coefficient of determination representing the goodness of a fit. The shell solidification factors K for **E1**, **E2**, **E3**, and **E4** are calculated as 1.24, 1.44, 1.43, and 1.54 $\text{mm s}^{1/2}$, respectively. Adj. R^2 , which is a value between 0 and 1, could be taken to evaluate the regular solidification of initial shell. Generally speaking, Adj. R^2 approximates 1 indicating a uniform solidification of initial shell. For example, Adj. R^2 is 0.98 and 0.91 for **E4** and **E1**, respectively, which suggests a more evenness solidification of **E4** shell than that of **E1** shell (Figure 3). Among those four trials, **E4** shell is the thickest one that could be attributed to the thinnest slag film infiltrated into the mold and shell gap which leads to a less thermal resistance to the heat transfer from the shell to the mold (see Figures 4, 5, and 10); thus, **E4** exhibits the highest heat flux among those

four trials (see Figure 8). Conversely, the **E1** infiltrated slag film is thickest, and hence its shell is the thinnest and its heat flux is the lowest (see Figures 3 and 8). However, shell solidification factor is 1.44 and 1.43 $\text{mm s}^{0.5}$ for **E2** and **E3** that are corresponding to the average slag film thickness of 1.20 and 0.86 mm, respectively. The abnormal in the shell thickness for **E3** case is probably associated with the higher crystal fraction appearing in **E3** slag film (Figure 6). Details of the relationship between the shell thickness, heat flux,

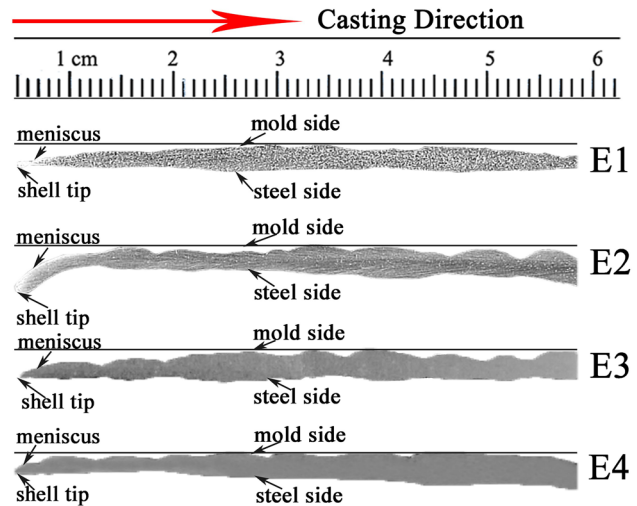


Fig. 3—The section profiles of initial solidification shells.

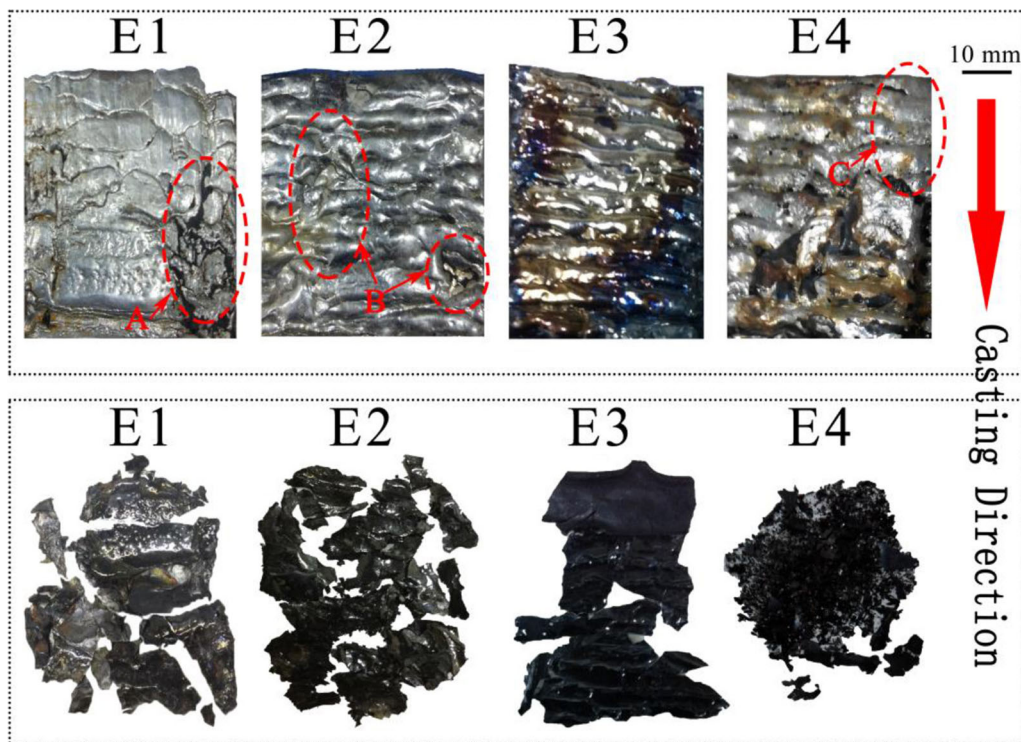


Fig. 2—(top) Shell surfaces from the mold simulator trials, and (bottom) the corresponding mold/shell slag films adjacent to the shell surface. **E1**, **E2**, **E3**, and **E4** corresponding to 5, 12, 20, and 25 minutes after adding mold flux on the top of molten steel, respectively.

the crystallization behavior, and thermal resistances of slag film will be discussed later.

C. Slag Film Thickness and Crystallization

As shown in Figure 5, the thickness of the infiltrated slag film along the centerline of mold is in the range of 1.58 to 3.41, 0.60 to 3.59, 0.37 to 2.47, and 0.30 to 2.15 mm for **E1**, **E2**, **E3**, and **E4**, respectively. The infiltrated slag film is observed to be thicker for the locations corresponding to oscillation marks and the surface depressions as well as for the location corresponding to the shell tip. The average thickness of the infiltrated mold/shell slag film for the distance 10 to 50 mm below the shell tip is calculated and listed in Table IV. The average slag film thickness is 2.02, 1.20, 0.86, and 0.57 mm for the trials **E1**, **E2**, **E3**, and **E4** that are corresponding to the slag viscosity of 0.35, 0.47, 0.58, and 0.76 Pa s and slag basicity of 1.02, 1.04, 1.07, and 1.10, respectively. The results suggest the thickness of the infiltrated slag film decreases with the increase of slag viscosity and basicity.

Therefore, a lower viscosity and basicity of mold flux would result in a thicker infiltrated mold/shell slag film and the irregular slag infiltration that eventually leads to the irregular solidification of initial shell with a poor surface quality, such as slag entrapment and depressions as well as glaciation marks. Conversely, a higher viscosity and basicity of mold flux would result in a thinner infiltrated slag film, and cause the poor mold lubrication, which eventually leads to the longitudinal shell surface defects, drag marks, *etc.* Hence, there would be an optimum viscosity and basicity range for good performance of slag infiltration and lubrication, such that the regular solidification of initial shell with a good surface quality would be obtained. Details of slag consumptions and lubrication will be discussed later.

Figure 6 shows the SEM images of the slag film obtained from **E1**, **E2**, **E3**, and **E4** trials at 6 mm (upper), 28 mm (middle), and 42 mm (lower) below the shell tip. For trial **E1**, distinct crystallization characteristics could be observed from the upper to lower part of the slag film. The crystal fraction appearing in the lower

part was higher than that in the upper part of slag film where the fraction of crystalline phases is 68.7, 76.6, and 94.6 pct for the location 6, 28, and 42 mm below the shell tip, due to the fact that the slag in the lower part experiencing a longer time to crystallize. When the reaction time was extended to 12 minutes, the content of Al_2O_3 was increased to 10.34 pct in **E2** trial, and the fraction of crystalline phases is 70.0, 77.9, and 95.7 pct for the location 6, 28, and 42 mm below the shell tip, respectively. While the equiaxed crystals became quite common in **E2** slag film compared with **E1** case, as **E2** slag has a higher viscosity and crystallization tendency due to the increase of wt pct Al_2O_3 and CaO/SiO_2 ratio.^[6,7,38] For **E3** slag, the fraction of crystalline phases is 70.0, 79.0, and 95.8 pct for the location 6, 28, and 42 mm below the shell tip, respectively. However, big primary crystal dendrites were observed to grow along the direction of heat transfer from the shell toward the mold. This is due to the increased tendency of mold flux crystallization and the huge temperature gradient between mold and shell that may be associated with the increased viscosity and basicity. For the case of **E4**, the infiltrated slag film was thinnest as 0.57 mm, and the viscosity of liquid slag was highest among those four slags of **E1**, **E2**, **E3**, and **E4** which the viscosity is three times of the original mold flux. Therefore, the temperature gradient within the gap between the mold and initial shell would be extremely high, which would in turn result in a largest cooling rate for this case; thus, the majority part of the mold flux would be changed into glassy phase. The glassy phase was also clearly observed in **E4** slag film (Figure 2), where it was broken into pieces during the process of cutting of the shell away from the mold.

In sum, the thickness of infiltrated mold/shell slag film decreases with increasing both viscosity and basicity of slag caused by the reaction between liquid slag and molten steel during continuous casting. The crystallization of the infiltrated mold/shell slag film is dynamic along the casting direction. The crystal morphology of infiltrated slag film is the result of the combined effect of the slag chemical composition, cooling rate, and viscosity. Generally speaking, crystals prefer to oriented growth, and the crystal fraction increases with increasing weight percentage of Al_2O_3 and CaO/SiO_2 ratio, *i.e.*, **E1** to **E3** slag films. Meanwhile, the slag film will form glass phase if the cooling rate is high enough, *i.e.*, **E4**.

D. Heat Transfer of Mold

The measured mold temperatures during casting were delivered into 2D-IHCP,^[33] and then the heat flux and temperature of the mold surface were determined. Figure 7 shows the recovered temperatures of mold hot face at 7 mm below the shell tip during casting time, and the responding temperatures were about 340 K to 372 K, 362 K to 384 K, 360 K to 381 K, and 391 K to 428 K for **E1**, **E2**, **E3**, and **E4**, respectively. The mold hot face temperature in the **E4** trial is the highest, followed by the case of **E2**, **E3**, and **E1**. The detailed description of the variation of mold hot face temperatures could be found in previous studies.^[29,30]

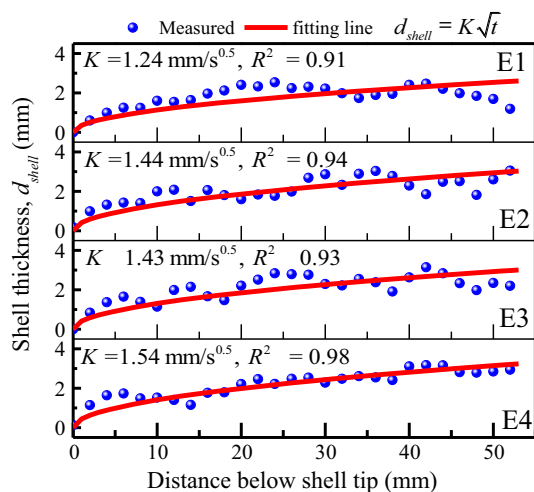


Fig. 4—The measured shell thickness.

Figure 8 shows the heat fluxes across the mold hot face at 7 mm below the shell tip during continuous casting. The heat fluxes are fluctuating around the

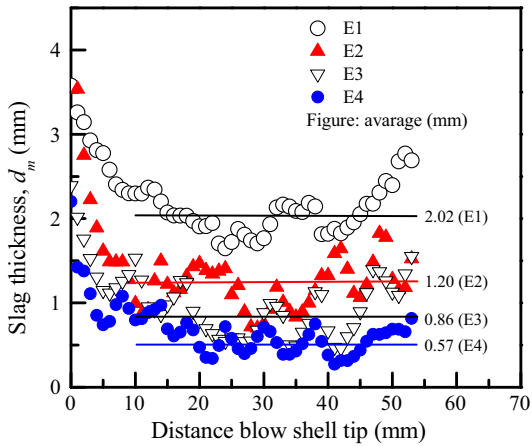


Fig. 5—Thickness of slag film between the mold and the shell.

baseline of 1.17, 1.57, 1.47, and 2.07 MW/m² for **E1**, **E2**, **E3**, and **E4**, respectively, and these average values are listed in Table IV. There are two major effects of slag-steel reaction on the mold heat flux and temperature. First, the thickness of infiltrated mold/shell slag film decreases with increasing viscosity and basicity of mold flux caused by the process of metal-slag reaction. A thicker slag film will lead to a higher thermal resistance to the heat transfer from the shell to the mold (Figure 10).^[17,39,40] If the effect of slag film thickness prevails, the heat flux, mold surface temperature, and the shell solidification factor would increase with decreasing the slag film thickness. For example, the average heat flux is 1.17, 1.57, and 2.07 MW/m², the shell solidification factor is 1.22, 1.44, and 1.54 mm s^{0.5}, and the mean temperature of mold surface is 361 K, 382 K, and 413 K for the case of **E1**, **E2**, and **E4**, which are corresponding to the average slag film thickness of 2.02, 1.20, and 0.57 mm, respectively. For the other issue, the crystal fraction of slag film increases with increasing weight percentage of Al₂O₃ and CaO/SiO₂ ratio as the progress of continuous casting. Although **E3**

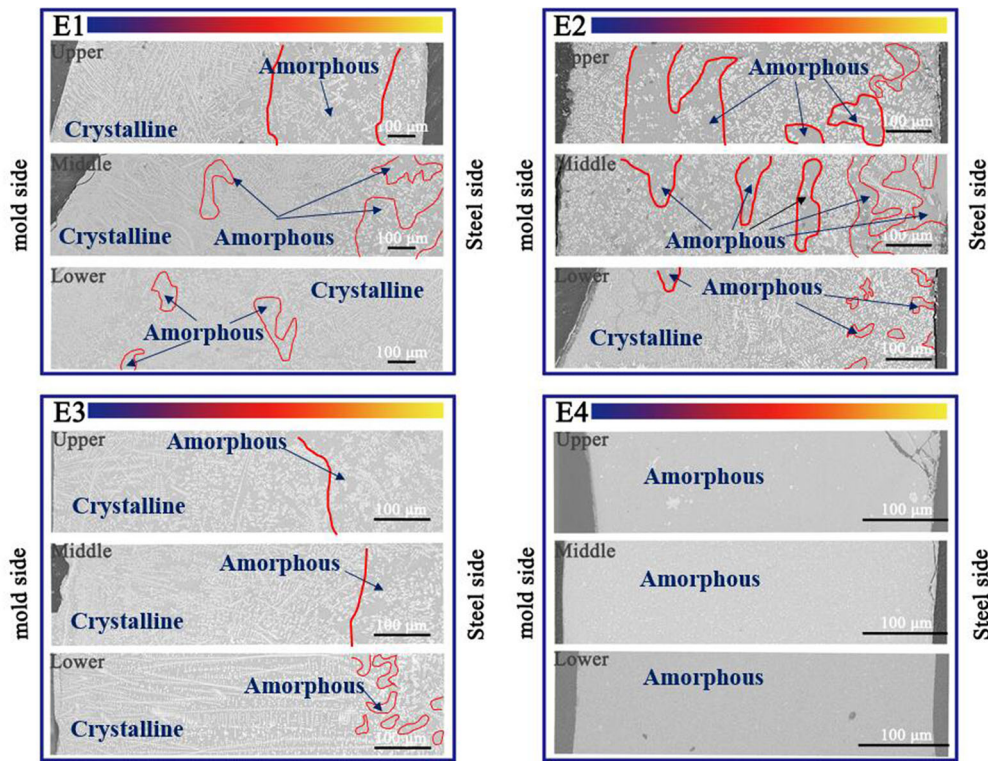


Fig. 6—SEM image of the slag film taken between the mold and the shell at different locations below the meniscus for the trials of **E1**, **E2**, **E3**, and **E4**, where upper, middle, and lower mean the locations of 6, 28, and 42 mm below the shell tip, respectively.

Table IV. Experimental Heat Flux, Temperature, Slag Thickness, and Shell Solidification Factor

Trial	E1	E2	E3	E4
Mean heat flux at meniscus area and its <i>standard deviation</i> (MW/m ²)	1.17, 0.23	1.57, 0.19	1.47, 0.18	2.07, 0.14
Mean mold surface temperature (K)	361	382	377	413
<i>K</i> -factor (mm s ^{0.5}) and <i>Adj. R</i> ²	1.24, 0.91	1.44, 0.94	1.43, 0.93	1.54, 0.98
Average thickness of slag film (mm)	2.02	1.20	0.86	0.57

slag film is slight thinner compared with **E2** slag film, when the effect of crystallization predominates, the **E3** slag film will exert more thermal resistances to heat transfer from the shell to the mold (Figure 10), and then the overall **E3** mold heat flux during the time from 1.75 to 3.5 seconds is lower than that of **E2**. Thus, the shell solidification factor ($1.43 \text{ mm s}^{0.5}$) and the mean temperature of mold hot face (377 K) for **E3** are slightly lower than the case of **E2**. It also needs to be noted that the drop of heat flux during the late stage of casting period from 1.75 to 3.5 seconds in **E3** might be due to the increase of slag film thickness caused by the deformation of initial shell (Figures 3 and 5).

Therefore, the overall heat transfer rate and solidification factor are determined by both the slag film thickness and the crystallization fraction in the solid slag film. The standard deviation of heat flux is 0.23, 0.19, 0.18, and 0.14 MW/m^2 and the fluctuation rate of heat flux is 19.66 pct (0.23/1.17), 12.10 pct (0.19/1.57), 12.24 pct (0.18/1.47), and 6.76 pct (0.14/2.07) for **E1**, **E2**, **E3**, and **E4**, respectively, where the corresponding Adj. R^2 of shell thickness curve fitting is 0.91, 0.94, 0.93, and 0.98,

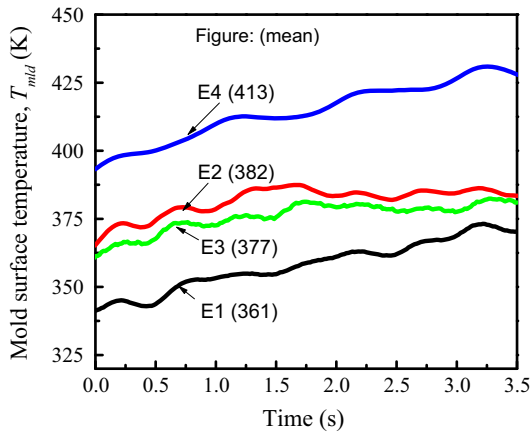


Fig. 7—Responding temperatures of mold surface at the meniscus area during casting time.

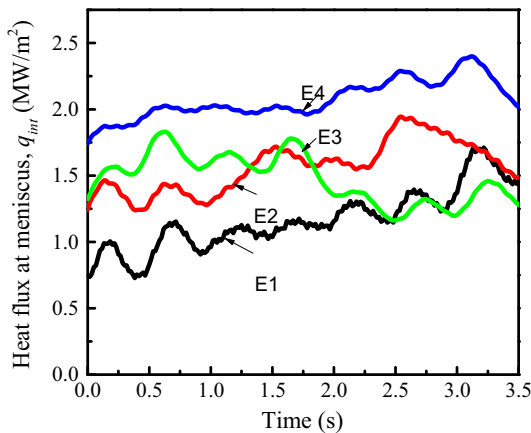


Fig. 8—Heat fluxes across the mold hot face in the meniscus area during casting time.

respectively. It implies that a fluctuating heat flux at meniscus area would lead to the uneven solidification of initial shell.

E. Heat Transfer and Lubrication Behavior of Slag Film

Figure 9 shows the thermal resistances between the mold and the shell. The total thermal resistance R_{tot} between shell and mold includes the mold/slag interfacial thermal resistance R_{int} , the solid slag film thermal resistance R_s , and the liquid slag film thermal resistance R_l .

For simplification, the process of heat transfer in the slag film is assumed^[40]: (1) the liquid slag temperature at shell side equals to the shell surface temperature, (2) the latent heat during the solid-liquid transition of liquid slag film is neglected, and (3) the heat transfer in slag film is assumed to be a steady state, owing to the fact that the heat transfers from the shell to the mold q_{int} is much larger than of heat accumulated in slag film. According to the superposition principle, the mold surface heat flux (q_{int}) would be regarded as the horizontal component of heat flux across the slag film. Therefore, the total thermal resistance R_{tot} between shell and mold, mold/slag interfacial thermal resistance R_{int} , solid slag film thermal resistance R_s and liquid slag film thermal resistance R_l as well as the shell surface temperature T_{sh} , and slag surface temperature T_{ss} could be estimated from the average mold surface heat flux q_{int} , liquidus of the steel T_{liq} , crystallization temperature of mold flux T_{sol} , and the average mold surface temperature T_{mld} , that is,

$$\begin{aligned} q_{\text{int}} &= \frac{T_{\text{sh}} - T_{\text{mld}}}{R_{\text{tot}}} = \frac{T_{\text{ss}} - T_{\text{mld}}}{R_{\text{int}}} = \frac{T_{\text{sol}} - T_{\text{ss}}}{R_s} \\ &= \frac{T_{\text{sh}} - T_{\text{sol}}}{R_l} = \frac{k_{\text{steel}}}{d_{\text{shell}}} (T_{\text{liq}} - T_{\text{sh}}), \end{aligned} \quad [3]$$

where R_{tot} ($= R_{\text{int}} + R_s + R_l$) is thermal resistances between mold/shell, k_{steel} is the thermal conductivity of steel, d_{shell} is shell thickness.

The liquid slag film thermal resistance R_l consists of the conductive thermal resistance R_{lc} and the radiative thermal resistance $1/h_{\text{lr}}$, that is,

$$R_l = \frac{1}{1/R_{\text{lc}} + h_{\text{lr}}}, \quad [4]$$

where R_{lc} equals to d_l/k_{sl} , and the radiative thermal resistance is as follows:^[10]

$$\frac{1}{h_{\text{lr}}} = \frac{0.75a_l d_l + \varepsilon_{\text{sh}}^{-1} + \varepsilon_{\text{cry}}^{-1} - 1}{m^2 \sigma_B (T_{\text{sh}}^2 + T_{\text{sol}}^2)(T_{\text{sh}} + T_{\text{sol}})}. \quad [5]$$

By knowing R_l , T_{sh} , and T_{sol} , the liquid slag film thickness d_l is calculated from Eqs. [4] and [5], and then the solid slag film thickness d_s could be obtained from the measured slag film thickness d_m ,

$$d_s = d_m - d_l. \quad [6]$$

The liquid slag acts as lubrication function for mold/shell and its consumption per unit area of shell surface

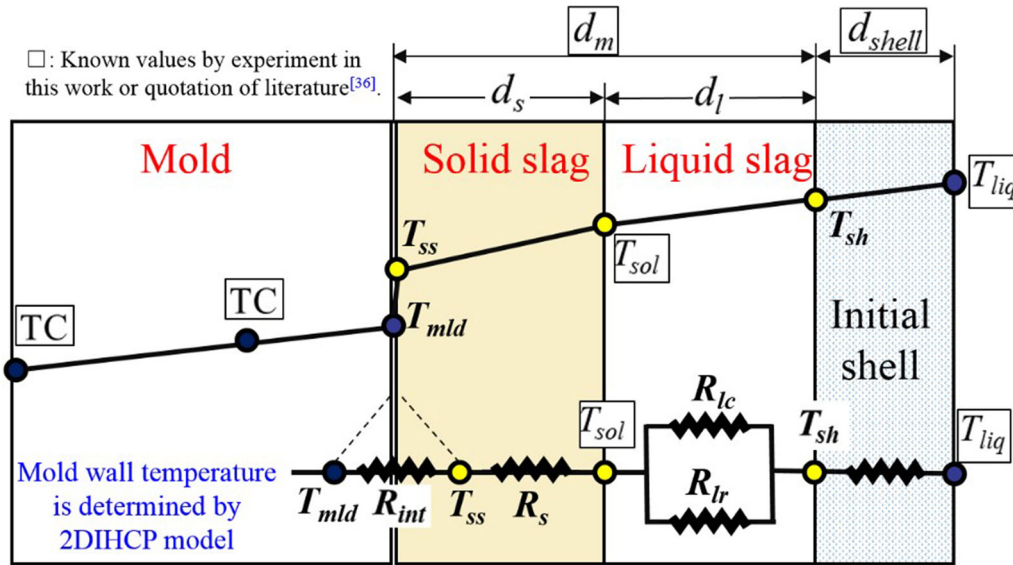


Fig. 9—Heat transfer model across the infiltrated mold/shell slag film.

(Q_{slag}) could be estimated by Thomas-Meng expression^[41] once the liquid slag film thickness (d_l), the downward velocity of solid slag film (V_s), and liquid slag film (V_l) are given.

$$Q_{slag} = \frac{f\rho_{slag}}{V_c} \int_0^{1/f} \left(\int_0^{d_l} V_l dx + V_s d_s \right) dt, \quad [7]$$

where the solid slag film in the vicinity of meniscus area can be assumed to stick to the mold wall,^[42] so V_s equals to $2\pi f A \cos(2\pi f t)$ and the liquid slag film (V_l) is

$$V_l = \frac{-(\rho_{slag} - \rho_{steel})gx^{n+2}}{\mu_s(n+2)d_1^n} + \left(\frac{V_c - V_s}{d_l} + \frac{(\rho_{slag} - \rho_{steel})gd_1}{\mu_s(n+2)} \right) \frac{x^{n+1}}{d_1^n} + V_s, \quad [8]$$

where x is the horizontal distance between the crystal/liquid slag interface and a point within liquid slag film, ρ_{slag} is the density of slag, ρ_{steel} is the density of steel, g is the acceleration of gravity, $\mu_s (= \mu_0 \times [(1300 - T_{sol})/(T - T_{sol})]^n)$ is the slag viscosity, μ_0 is the viscosity of slag at 1300 °C, and n is the temperature-dependent viscosity exponent.

In this study, the location 7 mm below the shell tip was chosen for the characterization of the heat transfer and lubrication behavior of infiltrated mold/shell slag film, where the maximum heat flux across the mold is located at this position. Then the average heat flux (q_{int_7}) and temperature (T_{mld_7}) of mold surface at 7 mm below the shell tip during the last mold oscillation cycle (from 3.0 to 3.5 seconds) when continuous casting is completing (Figures 7 and 8) are calculated and listed in Table V. Also, the measured thickness of shell (d_{shell_7}) and infiltrated mold/shell slag film (d_{m_7}) at 7 mm below the shell tip (Figures 4 and 5) are listed in Table V. The local average heat flux q_{int_7} is 1.56, 1.64, 1.36, and 2.25 MW/m², and the local average

temperature T_{mld_7} is 371.47, 384.96, 380.83, and 426.51 K for **E1**, **E2**, **E3**, and **E4**, respectively. R_{tot} , R_{int} , R_s , R_l , T_{sh} , T_{ss} , d_s , d_l , and Q_{slag} at 7 mm below the shell tip are calculated from Eqs. [3] through [8]). During the calculation, the physical properties of mold flux and steel, e.g., shell emission ϵ_{sh} , thermal conductivity T_{sol} , are listed in Table VI.^[7,13,37,43–46]

1. Heat transfer behavior

Generally speaking, a thicker slag film between mold and shell would lead to a higher thermal resistance to the heat transfer from the shell to the mold.^[9] As Figure 10 shows, the total mold/shell thermal resistance R_{tot} of the location 7 mm below the shell tip is 8.87×10^{-4} , 8.28×10^{-4} , and 5.72×10^{-4} m² K/W for **E1**, **E2**, and **E4** that are corresponding to the local slag film thickness (d_{m_7}) of 2.34, 1.49, and 1.08 mm, respectively. Although the local slag film thickness of **E3** (1.25 mm) is smaller than that of **E2** (1.49 mm), R_{tot} of **E3** (10.11×10^{-4} m² K/W) is higher than that of **E2** (8.28×10^{-4} m² K/W) at 7 mm below the shell tip, which is due to a higher crystal fraction of **E3** slag (Figure 6) introducing more thermal barriers to the heat transfer.^[10–16]

Moreover, the percentage of the solid slag film thermal resistance R_s , the liquid slag film thermal resistance R_l , and the mold/slag interfacial thermal resistance R_{int} over the total mold/shell thermal resistance are 53.00 to 63.48 pct (R_s/R_{tot}), 15.55 to 23.65 pct (R_l/R_{tot}), and 20.97 to 23.81 pct (R_{int}/R_{tot}), respectively. It could be observed the thermal resistance in slag film ($R_s + R_l$) is larger than the mold/slag interfacial thermal resistance R_{int} for the location 7 mm below the shell tip. The thickness and crystallinity of slag film had a significant effect on R_s . The thermal resistance of solid slag film R_s at 7 mm below the shell tip is 3.63×10^{-4} , 4.70×10^{-4} , 4.74×10^{-4} , and 5.83×10^{-4} m² K/W for **E4**, **E1**, **E2**, and **E3** that are corresponding to the local solid slag film thickness of 0.96, 1.99, 1.23, and 0.92 mm

Table V. Inputting Data for the Heat Transfer Model of Infiltrated Mold/Shell Slag

Data	E1	E2	E3	E4
Average mold surface temperature during the last mold oscillation cycle, T_{mld_7} (K)	371.47	384.96	380.83	426.51
Average mold heat flux during the last mold oscillation cycle, q_{int_7} (MW/m ²)	1.56	1.64	1.36	2.25
Measured shell thickness, d_{shell_7} (mm)	1.24	1.40	1.38	1.48
Measured slag film thickness, d_{m_7} (mm)	2.34	1.49	1.25	1.08

Table VI. Physical Properties of Mold Flux

Parameters	Value	Unit
Shell emission ϵ_{sh}	0.78 ^[37]	—
Crystalline slag emission ϵ_{cry}	0.7 ^[13]	—
Slag refractive index m	1.6 ^[43]	—
Stefan–Boltzmann constant σ_B	5.6705×10^{-8}	W/(m ² K ⁴)
Absorption coefficient of liquid slag a_l	400 ^[44,45]	m ⁻¹
Slag density ρ_{slag}	2500 ^[7]	kg/m ³
Steel density ρ_{steel}	7400	kg/m ³
liquidus of the steel, T_{liq}	1811 K	
Thermal conductivity of air k_a	0.032	W/m K
Thermal conductivity of steel k_{steel}	34	W/m K
Thermal conductivity of liquid slag k_{sl}	1.2 ^[46]	W/m K

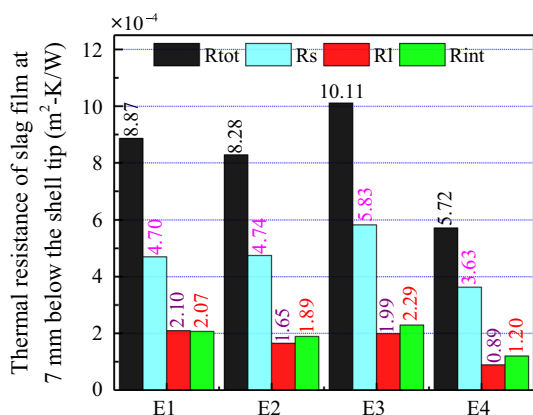


Fig. 10—Thermal resistance of slag film at 7 mm below the shell tip.

(Figure 11), respectively. R_s of **E3** is larger than that of **E2**, although the local solid slag film thickness of **E3** (0.92 mm) is smaller than that of **E2** (1.23 mm), which is due to the crystal fraction of **E3** slag film being the highest among the cases of **E1**, **E2**, **E3**, and **E4** (Figure 6).

In addition, Eqs [4] and [5] show that the thermal resistance (R_l) and thickness (d_l) of liquid slag film are the function of the slag crystallization temperature (T_{sol}), surface temperature of solidifying shell (T_{ss}), and mold slag properties. R_l at 7 mm below the shell tip is 2.10×10^{-4} , 1.65×10^{-4} , 1.99×10^{-4} , and 0.89×10^{-4} m² K/W, and d_l is 0.35, 0.26, 0.33, and 0.12 mm for the trials of **E1**, **E2**, **E3**, and **E4** that are corresponding to the local average mold heat flux (q_{int_7}) of 1.56, 1.64, 1.36, and 2.25 MW/m², respectively.

Both thickness and crystallinity of the slag film have effect on the mold/slag interfacial thermal resistance R_{int} . R_{int} of the location 7 mm below the shell tip is 2.07×10^{-4} , 1.89×10^{-4} , 2.29×10^{-4} , and

1.20×10^{-4} m² K/W for **E1**, **E2**, **E3**, and **E4** that are corresponding to the local slag film thickness (d_{m_7}) of 2.34, 1.49, 1.25, and 1.08 mm, respectively. R_{int} for **E3** (2.29×10^{-4} m² K/W) is higher than that of **E2** (1.89×10^{-4} m² K/W) although the local slag film thickness of **E3** (1.25 mm) is smaller than that of **E2** (1.49 mm), which is due to a higher crystal fraction in **E3** slag film than that of **E2** slag film (Figure 6). Supposing that R_{int} is the result of the air gap formation between the mold and the slag film, Figure 12 shows that the equivalent air gap size ($R_{int} \times k_a$) could be calculated as 6.6, 6.0, 7.3, and 3.8 μ m for **E1**, **E2**, **E3**, and **E4**, respectively. The air gap tends to increase with slag thickness. Also the abnormal of air gap size for **E3** case in comparison with the cases of **E1**, **E2**, and **E4** is associated with the highest crystal fraction appearing in **E3** slag film (Figure 6).

2. Lubrication behavior

The calculated liquid slag consumptions Q_{slag} are 0.2606, 0.1853, 0.2502, and 0.1034 kg/m² for **E1**, **E2**, **E3**, and **E4** that are corresponding to the mold flux viscosity at 1573 K (1300 °C) of 0.35, 0.47, 0.58, and 0.76 Pa s, respectively. Generally speaking, the slag with higher viscosity would result in less liquid slag consumption (deteriorates mold lubrication).^[9,47,48] The viscosity of **E3** mold flux is higher than that of **E2** (Figure 2) and the local slag film thickness of **E3** (1.25 mm) is smaller than that of **E2** (1.49 mm). However, **E3** shell has a better surface quality than that of **E2**, and the liquid slag consumption of **E3** (0.2502 kg/m²) is larger than that of **E2** (0.1853 kg/m²). The reason for this may be associated with the higher crystallinity of **E3** compared with **E2** case (Figure 6) that makes a larger total mold/shell thermal resistance R_{tot} (8.28×10^{-4} for **E2** vs 10.11×10^{-4} for **E3** m² K/W), and then a lower heat flux (1.64 for **E2** vs 1.36 MW/m² for **E3**) and a hotter

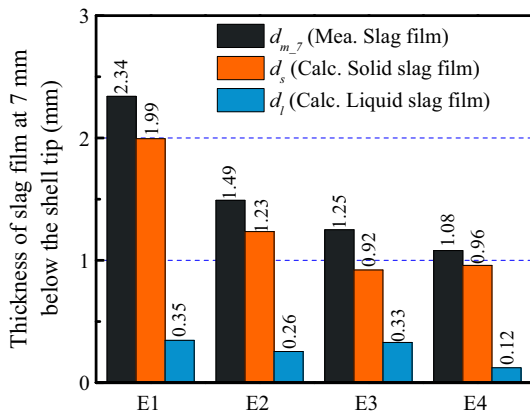


Fig. 11—Thickness of solid and liquid slag film at 7 mm below the shell tip.

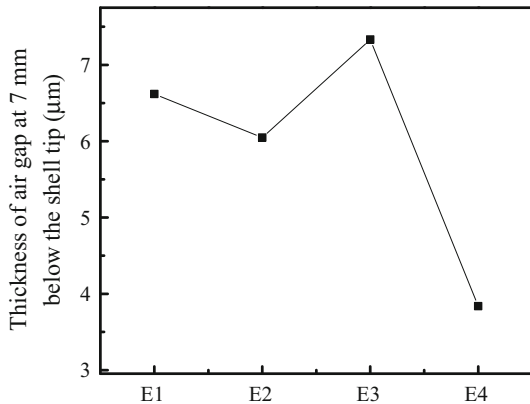


Fig. 12—Thickness of air gap at 7 mm below the shell tip.

shell surface temperature, thus a wider liquid slag film (0.26 for **E2** vs 0.33 mm for **E3**), and eventually a better lubrication for mold and shell as well as a better shell surface quality for **E3** case in comparison with **E2** case (Figure 2).

In summary, a lower viscosity and basicity of mold flux would result in a larger liquid slag consumption that tends to lead an irregular solidification of initial shell with a poor surface quality, such as slag entrapment and depressions as well as glaciation marks (see **E1** case). Conversely, a higher viscosity and basicity of mold flux would result in a smaller liquid slag consumption that introduces the poor mold lubrication, which eventually leads to the longitudinal shell surface defects, drag marks, *etc.* (see **E4** case). One strategy used to obtain a better shell surface quality is to select an optimal combination of slag properties (for instance, good **E3** shell surface) considering the effects of slag viscosity and basicity (determines T_{sol} and break temperature T_{br}), even more factors such as casting temperature, casing speed, mold frequency, *etc.* This strategy is consistent with work by Sridhar *et al.*,^[49] where they also put out a diagram for the selection of casting speed, viscosity, and break temperature of slag so as to minimize the

occurrences of shell surface cracks and mold sticker breakout.

IV. CONCLUSION

In the present work, the effect of reaction between liquid mold flux and molten steel on the initial shell solidification as well as the heat transfer and lubrication behavior of the infiltrated mold/shell slag film during the continuous casting of IF steel has been studied. The specific conclusions are made as follows:

1. The thickness of infiltrated mold/shell slag film decreases with increasing the viscosity and basicity of slag, due to the addition of weight percentage of Al_2O_3 and CaO/SiO_2 ratio in mold flux with the progress of the reaction between liquid slag and molten steel during continuous casting.
2. Slag-steel reaction has two major effects on the initial shell solidification of molten steel: one is increasing the mold heat flux and shell thickness by the decrease of slag film thickness as the viscosity and basicity of mold flux increases with the extension of the reaction. The other is the reduction of mold heat flux by the increase of crystal fraction in slag film as the weight percentage of Al_2O_3 and CaO/SiO_2 ratio increase with the progress of the slag-metal reaction.
3. A lower viscosity and basicity of mold flux would result in a larger liquid slag consumption that tends to lead to the irregular solidification of initial shell with a poor surface quality, such as slag entrapment and depressions as well as glaciation marks. Conversely, a higher viscosity and basicity of mold flux would result in a smaller liquid slag consumption that tends to cause the poor mold lubrication, which eventually leads to the longitudinal shell surface defects, drag marks, *etc.* Thus, an optimum selection of viscosity and basicity (determines T_{sol} and T_{br}) is essential for the good performance of slag infiltration and lubrication.

ACKNOWLEDGMENTS

The financial support from the National Natural Science Foundation of China (51528402, 51661130154, 51704333), and Newton Advanced Fellowship (NA150320) is greatly acknowledged.

REFERENCES

1. K.C. Mills and A.B. Fox: *ISIJ Int.*, 2003, vol. 43, pp. 1479–86.
2. G.A. Bezuidenhout and P.C. Pistorius: *Ironmak. Steelmak.*, 2000, vol. 27, pp. 387–91.
3. J.A. Kromhout: Ph.D. Dissertation, Technische Universiteit Delft, Netherlands, 2011, pp. 10–29.
4. M.A. Van Ende and I.H. Jung: *ISIJ Int.*, 2014, vol. 54, pp. 489–95.
5. H. Todoroki, T. Ishii, K. Mizuno, and A. Hongo: *Mater. Sci. Eng. A*, 2005, vol. 413, pp. 121–28.

6. K.C. Mills, S. Karagadde, P.D. Lee, L. Yuan, and F. Shahbazian: *ISIJ Int.*, 2016, vol. 56, pp. 264–73.
7. K.C. Mills: *ISIJ Int.*, 2016, vol. 56, pp. 1–3.
8. P.E. Ramirez-Lopez, P.D. Lee, K.C. Mills, and B. Santillana: *ISIJ Int.*, 2010, vol. 50, pp. 1797–1804.
9. K.C. Mills and C.A. Däcker: *The Casting Powders Book*, Springer International Publishing, 2017, pp. 446–46.
10. S. Ozawa, M. Susa, T. Goto, R. Endo, and K.C. Mills: *ISIJ Int.*, 2006, vol. 46, pp. 413–19.
11. H. Nakada, M. Susa, Y. Seko, M. Hayashi, and K. Nagata: *ISIJ Int.*, 2008, vol. 48, pp. 446–53.
12. W. Wang, L. Zhou, and K. Gu: *Met. Mater. Int.*, 2010, vol. 16, pp. 913–20.
13. K. Gu, W. Wang, L. Zhou, F. Ma, and D. Huang: *Metall. Mater. Trans. B*, 2012, vol. 43B, pp. 937–45.
14. M. Susa, A. Kushimoto, R. Endo, and Y. Kobayashi: *ISIJ Int.*, 2011, vol. 51, pp. 1587–96.
15. H. Shibata, K. Kondo, M. Suzuki, and T. Emi: *ISIJ Int.*, 1996, vol. 36 (Suppl), pp. S179–82.
16. K. Tsutsumi, T. Nagasaka, and M. Hino: *ISIJ Int.*, 1999, vol. 39, pp. 1150–59.
17. J.W. Cho, H. Shibata, T. Emi, and M. Suzuki: *ISIJ Int.*, 1998, vol. 38, pp. 440–46.
18. H. Nakada and K. Nagata: *ISIJ Int.*, 2006, vol. 46, pp. 441–49.
19. H. Mizuno, H. Esaka, K. Shinozuka, and M. Tamura: *ISIJ Int.*, 2008, vol. 48, pp. 270–76.
20. A. Yamauchi, K. Sorimachi, and T. Yamauchi: *Ironmak. Steelmak.*, 2002, vol. 29, pp. 203–07.
21. M. Hanao, M. Kawamoto, and A. Yamanaka: *ISIJ Int.*, 2012, vol. 52, pp. 1310–19.
22. P. Duvvuri, B. Petrus, and B.G. Thomas: *AISTech 2014*, Indianapolis, 2014.
23. J.W. Cho, K. Blazek, M. Frazee, H. Yin, J.H. Park, and S.W. Moon: *ISIJ Int.*, 2013, vol. 53, pp. 62–70.
24. J.W. Cho, S. Yoo, M.S. Park, J.K. Park, and K.H. Moon: *Metall. Mater. Trans. B*, 2017, vol. 48B, pp. 187–96.
25. A. Badri, T.T. Natarajan, C.C. Snyder, K.D. Powers, F.J. Mannion, and A.W. Cramb: *Metall. Mater. Trans. B*, 2005, vol. 36B, pp. 355–71.
26. A. Badri, T.T. Natarajan, C.C. Snyder, K.D. Powers, F.J. Mannion, M. Byrne, and A.W. Cramb: *Metall. Mater. Trans. B*, 2005, vol. 36B, pp. 373–83.
27. J.Y. Park, E.Y. Ko, J. Choi, and I. Sohn: *Met. Mater. Int.*, 2014, vol. 20, pp. 1103–14.
28. E.Y. Ko, J. Choi, J.Y. Park, and I. Sohn: *Met. Mater. Int.*, 2014, vol. 20, pp. 141–51.
29. H. Zhang, W. Wang, F. Ma, and L. Zhou: *Metall. Mater. Trans. B*, 2015, vol. 46B, pp. 2361–73.
30. H. Zhang and W. Wang: *Metall. Mater. Trans. B*, 2016, vol. 47B, pp. 920–31.
31. P. Lyu, W. Wang, and H. Zhang: *Metall. Mater. Trans. B*, 2017, vol. 48B, pp. 247–59.
32. S.C. Moon: Ph.D. Dissertation, University of Wollongong, Wollongong, AU, 2015, pp. 116–31.
33. H. Zhang, W. Wang, and L. Zhou: *Metall. Mater. Trans. B*, 2015, vol. 46B, pp. 2137–52.
34. M.S. Kim, S. Lee, J.W. Cho, M.S. Park, H.G. Lee, and Y.B. Kang: *Metall. Mater. Trans. B*, 2013, vol. 44B, pp. 299–308.
35. Y. Liu, W. Wang, F. Ma, and H. Zhang: *Metall. Mater. Trans. B*, 2015, vol. 46B, pp. 1419–30.
36. Y. Kawai and Y. Shiraishi: *Handbook of Physico-Chemical Properties at High Temperatures*, Iron and Steel Institute of Japan, Tokyo, 1988.
37. L. Zhou, W. Wang, F. Ma, J. Li, J. Wei, H. Matsuura, and F. Tsukihashi: *Metall. Mater. Trans. B*, 2012, vol. 43B, pp. 354–62.
38. K.C. Mills: *ISIJ Int.*, 2016, vol. 56, pp. 14–23.
39. C. Yang, G. Wen, Q. Sun, and P. Tang: *Metall. Mater. Trans. B*, 2017, vol. 48B, pp. 1292–1307.
40. H. Zhang and W. Wang: *Metall. Mater. Trans. B*, 2017, vol. 48B, pp. 779–93.
41. Y. Meng and B.G. Thomas: *Metall. Mater. Trans. B*, 2003, vol. 34B, pp. 685–705.
42. Y. Meng and B.G. Thomas: *ISIJ Int.*, 2006, vol. 46, pp. 660–69.
43. M. Hayashi, M. Susa, T. Oki, and K. Nagata: *ISIJ Int.*, 1997, vol. 37, pp. 126–33.
44. W. Wang, K. Gu, L. Zhou, F. Ma, I. Sohn, D.J. Min, H. Matsuura, and F. Tsukihashi: *ISIJ Int.*, 2011, vol. 51, pp. 1838–45.
45. M. Susa, K.C. Mills, M.J. Richardson, R. Taylor, and D. Stewart: *Ironmak. Steelmak.*, 1994, vol. 21, pp. 279–86.
46. D.W. Yoon, J.W. Cho, and S.H. Kim: *Met. Mater. Int.*, 2015, vol. 21, pp. 580–87.
47. M. Kawamoto, T. Murakami, M. Hanao, H. Kikuchi, and T. Watanabe: *Ironmak. Steelmak.*, 2002, vol. 29, pp. 199–202.
48. K. Tsutsumi, H. Murakami, S. Nishioka, M. Tada, M. Nakada, and M. Komatsu: *Tetsu-to-Hagané*, 1998, vol. 84, pp. 617–24.
49. S. Sridhar, K.C. Mills, and S.T. Mallaband: *Ironmak. Steelmak.*, 2002, vol. 29, pp. 194–98.